Formation of a topological monopole lattice and its dynamics in three-dimensional chiral magnets

Seong-Gyu Yang,[1] Ye-Hua Liu,[2] and Jung Hoon Han[1],*

[1]*Department of Physics, Sungkyunkwan University, Suwon 16419, Korea*
[2]*Theoretische Physik, ETH Zurich, 8093 Zurich, Switzerland*

Topologically protected swirl of the magnetic texture known as the skyrmion has become ubiquitous in both metallic and insulating chiral magnets. Meanwhile the existence of its three-dimensional analog, known as the magnetic monopole, has been suggested by various indirect experimental signatures in MnGe compound. Although Ginzburg-Landau arguments in favor of the formation of a three-dimensional crystal of monopoles and antimonopoles have been put forward, no microscopic model Hamiltonian was shown to support such a phase. Here we present strong numerical evidence from Monte Carlo simulations for the formation of a rocksalt crystal structure of monopoles and antimonopoles in short-period chiral magnets. Real-time simulation of the spin dynamics suggests there is only one internal excitation mode in the monopole crystal state in the frequency range of several gigahertz for the material parameters of MnGe.

I. INTRODUCTION

Attempts to view building blocks of nature as topologically protected objects such as knots have been a fascinating feature of modern physical science. The knot theory of atoms advanced by Thomson (Lord Kelvin) [1] was re-incarnated by Skyrme as a topological quantum theory of hadrons in the early 1960s [2]. Although the topological interpretation of quantum numbers for elementary particles may not have been universally accepted in subatomic physics, the beauty of the idea has remained well within the physics community and, quite recently, found immense physical realization in several kinds of magnetic materials ranging from B20 metallic magnetic compounds [3–5], atomically thin magnetic layers [6], multiferroic insulators [7], to ferroelectrics [8]. The form of the topological matter, now called the skyrmion lattice, bears an excellent resemblance to the well-known vortex lattice in type-II superconductors [9] and shares the character of two dimensionality, extending its existence in a columnar fashion when the host material in which it is formed is three dimensional. The topological vortex and skyrmion lattices have both been observed successfully through the visualization technique of Lorentz microscopy [5,10].

In higher dimensions one is granted the exciting opportunity to create, observe, and manipulate topological objects not permitted in lower dimensions. For example, in three-dimensional Heisenberg magnets with a local unit magnetization vector $\mathbf{n_r}$, localized objects known as monopoles and antimonopoles with integer topological numbers may be formed. The number characterizing the object's topology is

$$\frac{1}{4\pi} \int_S du \, dv \, \mathbf{n_r} \cdot \left(\frac{\partial \mathbf{n_r}}{\partial u} \times \frac{\partial \mathbf{n_r}}{\partial v} \right) = m \in \text{integer}, \quad (1)$$

for a two-dimensional integration domain $\int_S$, parametrized by (u,v), enclosing the monopole center $\mathbf{R}$. In the current literature, the terms hedgehogs and antihedgehogs are used interchangeably with monopoles and antimonopoles, and we remind the readers that they both refer to identical topological objects defined by Eq. (1) with $m > 0$ and $m < 0$, respectively. There is another three-dimensional topological object advocated in the original paper by Skyrme [2] characterized by a topological number more complicated than Eq. (1). This is the original skyrmion structure, while its descendant in two dimensions was often called the baby skyrmion. Due to the abundant sightings of the two-dimensional baby skyrmion structure in magnets in recent years, it became customary to drop the qualifier and simply refer to the two-dimensional topological object as the "skyrmion." In this work we address the formation of the monopole topological object, unique to three dimensions, in a simple model of chiral magnets.

There are two classes of emergent magnetic monopoles known in condensed matter physics. One is the monopole in spin ice materials [11]; the other is the hedgehog found in chiral magnets [12,13] and in constricted geometries like nanowires [14]. Due to the high energetic cost of creating the hedgehog-type monopole in isolation, they must be created in reality as a monopole-antimonopole (MAM) pair, or as a crystal of such pairs forming a new kind of topological lattice unique to three dimensions in B20 compound. Such possibility was suggested theoretically [15] some time ago following the intriguing discovery of diffuse neutron scattering peaks in MnSi under high pressure [16], and was further corroborated in the calculation of Ref. [17]. Several recent Hall and Nernst effect experiments on MnGe crystal have boosted our confidence that such three-dimensional topological phase has already been realized in nature even at ambient pressure [12,13], while a more direct visual confirmation, analogous to the Lorentz microscopy imaging of the three-dimensional skyrmion lattice, may still be forthcoming [18]. A pressing issue for theory at this stage is to inquire if a simple magnetic model Hamiltonian supporting the MAM crystal phase can be written down, and used to address various aspects of the monopole crystal dynamics.

We show that a well-known three-dimensional model of Heisenberg spins interacting through short-range ferromagnetic and Dzyaloshinskii-Moriya (DM) exchanges of strengths
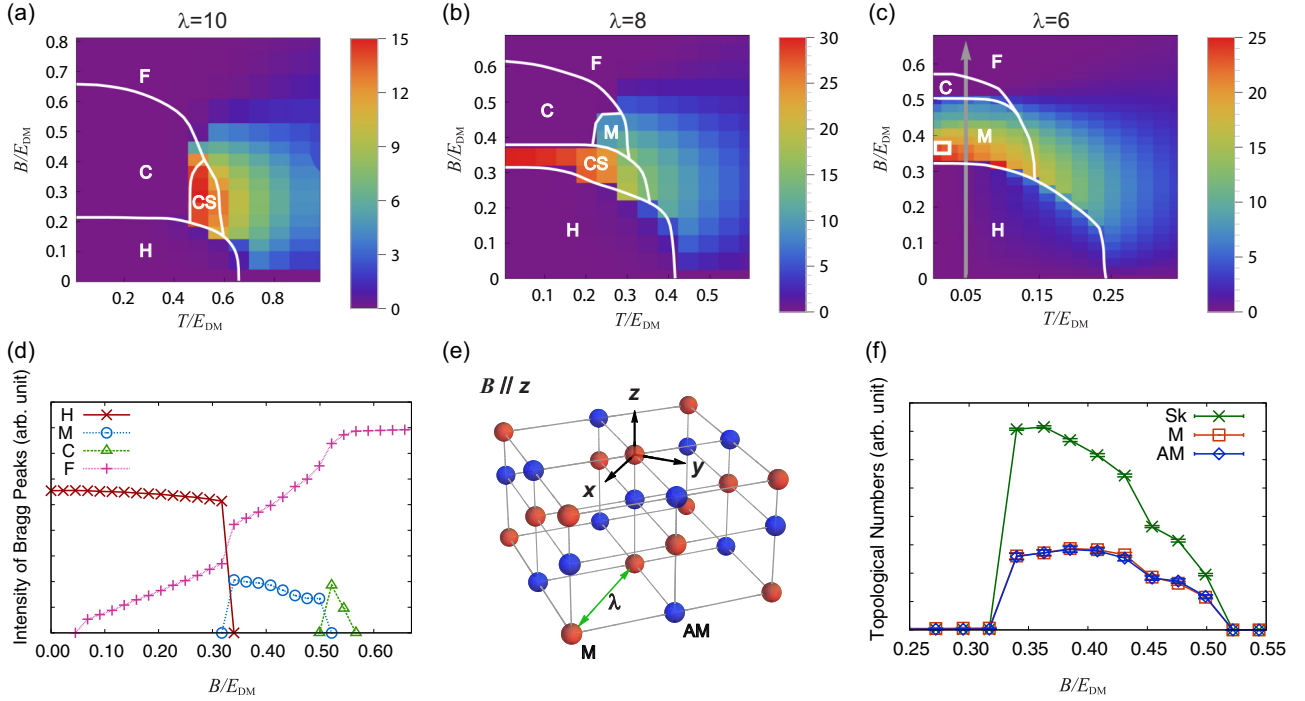
*hanjh@skku.edu

FIG. 1. Phase diagrams for increasing strengths of the Dzyaloshinskii-Moriya interaction. The wavelength of spin helix is set to (a) $\lambda = 10$, (b) $\lambda = 8$, and (c) $\lambda = 6$, respectively, with the lattice constant equal to unity. Color plots indicate the integrated skyrmion density $(1/4\pi) \int dx\, dy\, \mathbf{n} \cdot (\partial_x \mathbf{n} \times \partial_y \mathbf{n})$ within the xy plane, further averaged over all the layers in the z direction. An energy unit $E_{DM} = D^2/J$ is used to normalize the temperature and magnetic-field scales. Acronyms indicate helical (H), columnar skyrmion (CS), conical (C), ferromagnetic (F), and monopole-antimonopole crystal (M) phases, respectively. Phase boundaries are obtained from analyses of the Bragg peak intensities. (d) Intensity of Bragg peaks corresponding to different phases along the gray arrow in (c). Points denote the magnitude of $\mathbf{n_q}$ for each phase. As the magnetic field gets stronger, spins in the lattice are partially aligned along the z axis. (e) Rocksalt structure of the monopole-antimonopole crystal, at the location of the empty white square in the phase diagram (c). Red and blue balls represent monopoles and antimonopoles, respectively. (f) Variation of the skyrmion (Sk), monopole (M), and antimonopole (AM) topological numbers with increasing magnetic field at $\lambda = 6$ along the gray arrow in (c). All the topological numbers are averaged over all the layers with 300 000 MC steps of ensemble average. Monopoles and antimonopoles always occur in equal numbers. Magnetic-field dependencies of both topological numbers are similar. Statistical variations are less than the size of the symbols.

J and D, respectively, supports the MAM phase at a sufficiently short wavelength $\lambda/a \sim J/D$, where a is the lattice constant. The same model is known to give rise to the columnar skyrmion (CS) lattice phase within the so-called A-phase region of the phase diagram [19]. The small pocket occupied by the A phase expands to cover the entire low-temperature regime as the thickness of the sample is reduced below the helical wavelength [20]. We show, through extensive Monte Carlo (MC) simulations of the same three-dimensional lattice model, that at shorter periods of the helix the A phase gives way to the MAM crystal phase. The MAM phase (which we will also call the M phase) initially occurs around the high-temperature region just below the magnetic order and expands to cover the low-temperature region at a shorter helix period. In order to make the extensive three-dimensional simulation feasible we have developed an efficient Monte Carlo algorithm based on graphics processing units (GPUs) as explained in Sec. II C. Subsequent to the identification of the M phase we carry out the Landau-Lifshitz-Gilbert (LLG) simulation of the real-time spin dynamics in an effort to uncover the low-energy collective modes. Only one such mode could be identified well below the exchange energy scale J for the MAM crystal.

II. PHASE DIAGRAM

A. Results

Buhrandt and Fritz [19] were the first to explicitly demonstrate the existence of the A phase, nowadays identified with the CS phase, in their MC calculation for a three-dimensional model of chiral magnets. A phase diagram similar to theirs is shown in Fig. 1(a) (we use $\lambda = 10$ instead of $\lambda \sim 15$ as in their work). From there, we reduce the helix period λ by tuning the D/J ratio and observe the evolution of the phase diagram. Throughout the simulation the Zeeman field is applied along the positive z direction. As shown in Fig. 1(b) for $\lambda = 8$, the CS phase becomes stable even at very low temperatures where there used to be either the spiral or conical phase. One also starts to see the appearance of the M phase in a small pocket that used to be occupied by the A phase. For an even shorter wavelength $\lambda = 6$, the low-temperature CS phase entirely gives way to the M phase. As seen in Fig. 1(c), a succession of phase transitions, from helical (H) to M then followed by conical (C) and ferromagnetic (F) phases, occur with increasing magnetic field at a fixed, low temperature. In producing various phase diagrams we adopted reduced units, in which both the temperature T/E_{DM} and the magnetic field

B/E_{DM} are made dimensionless in terms of the energy scale $E_{DM} = D^2/J$.

To associate a given MC-generated spin configuration with a particular phase we Fourier analyze the equilibrium spin configuration $\mathbf{n_r}$ with

$$\mathbf{n_r} = \sum_{\mathbf{q}} \mathbf{n_q} e^{i\mathbf{q}\cdot\mathbf{r}}. \tag{2}$$

Examination of the Bragg intensities $|\mathbf{n_q}|^2$ yields the phase to which the spin configuration belongs. The MAM crystal state has four pairs of Bragg peaks located along $(1,0,1)$, $(-1,0,1)$, $(0,1,-1)$, and $(0,-1,-1)$ directions, as expected in the face-centered cubic (fcc) structure [15,17]. For the helical phase (H) a single pair of Bragg peaks occurs along the (111) direction, and for the conical phase (C) along the (001) direction. The columnar skyrmion phase (CS) has three pairs of $\mathbf{q}$ vectors in the q_x-q_y plane as is well known [3,4,19]. There is also a $\mathbf{q} = 0$ peak for all the phases due to the finite Zeeman field. The ferromagnetic phase (F) has only the $\mathbf{q} = 0$ peak.

Figure 1(d) shows the evolution of H, M, and C phases in terms of their respective Bragg intensities. Points in Fig. 1(d) are the magnitudes of $\mathbf{n_q}$ at the relevant wave vector $\mathbf{q}$. A clear phase boundary can be read off from the rise and fall of each intensity as a function of the magnetic field strength at a given temperature. To draw phase boundaries, we first identify points in the (B,T) phase diagram where the Bragg intensities vanish, then employ a numerical interpolation software to connect the dots into smooth phase boundaries shown as white lines in Figs. 1(a)–1(c). The white-lined phase boundaries obtained this way overlap quite well with the color background obtained from the skyrmion number calculation described in Sec. II B. MC calculations of thermodynamic quantities such as the specific heat and magnetic susceptibility offered compatible phase boundaries. Most of the phase boundaries we observe are of first order, and it proved to be most convenient to adopt the Bragg intensities as the appropriate order parameter and obtain the phase diagram in terms of them.

In the theoretical literature several possibilities for the monopole crystal structure were proposed, including the simple cubic, face-centered cubic, and body-centered cubic structures [15,17]. Among these proposals the one realized by the microscopic model we have adopted is the fcc structure. We confirm this by identifying monopole and antimonopole locations from the MC-generated spin configuration (as detailed in Sec. II B) and plotting them in real space. As shown in Fig. 1(e), monopoles and antimonopoles, respectively, form a fcc lattice and they together constitute a rocksalt structure. The monopole-monopole separation is equal to λ in the plane orthogonal to the Zeeman field and slightly less along the field direction. Accordingly, Bragg peak analysis of the spin structure in the M phase yields four noncoplanar peaks at $(2\pi/\lambda)(2,0,12/5)$, $(2\pi/\lambda)(-2,0,12/5)$, $(2\pi/\lambda)(0,2,-12/5)$, and $(2\pi/\lambda)(0,-2,-12/5)$, in conformity with the fcc structure.

B. Monopole number calculation

The topological charge density of skyrmions in two-dimensional magnets is measured by

$$[\rho_{sk}]_{2D} = \frac{1}{4\pi} \mathbf{n} \cdot (\partial_x \mathbf{n} \times \partial_y \mathbf{n}). \tag{3}$$

This is generalized in three-dimensional (3D) magnets as a vector of skyrmion densities,

$$[\rho_{sk}^\alpha]_{3D} = \frac{1}{8\pi} \varepsilon^{\alpha\beta\gamma} \mathbf{n} \cdot (\partial_\beta \mathbf{n} \times \partial_\gamma \mathbf{n}), \tag{4}$$

where each component measures the skyrmion density within the $(\beta\gamma)$ plane normal to the given direction $\alpha = x,y,z$. The divergence of the vector

$$\rho_m = \partial_\alpha [\rho_{sk}^\alpha]_{3D} \tag{5}$$

then measures the monopole density in the magnetic structure [21,22]. For the typical monopole and antimonopole configurations $\mathbf{n_r} = \pm\mathbf{r}/r$, one obtains $\rho_m = \pm\delta(\mathbf{r})$ by explicit calculation.

In the discretized lattice model, certain well-defined procedures can be employed to calculate the skyrmion and monopole numbers. To calculate the skyrmion density at a certain lattice position $\mathbf{r}$, we choose four triangles spanned by the triplet of lattice sites $\{\mathbf{r}+\hat{x}, \mathbf{r}+\hat{y}, \mathbf{r}-\hat{y}\}$, $\{\mathbf{r}+\hat{y}, \mathbf{r}-\hat{x}, \mathbf{r}+\hat{x}\}$, $\{\mathbf{r}-\hat{x}, \mathbf{r}-\hat{y}, \mathbf{r}+\hat{y}\}$, and $\{\mathbf{r}-\hat{y}, \mathbf{r}+\hat{x}, \mathbf{r}-\hat{x}\}$, and compute the solid angle for each triangle. The solid angle calculation is done with the well-known formula [23]

$$\Omega = 2\arctan\left[\frac{\mathbf{a}\cdot(\mathbf{b}\times\mathbf{c})}{1+\mathbf{a}\cdot\mathbf{b}+\mathbf{b}\cdot\mathbf{c}+\mathbf{c}\cdot\mathbf{a}}\right], \tag{6}$$

where Ω is the solid angle, and $\mathbf{a}$, $\mathbf{b}$, and $\mathbf{c}$ are the unit vectors of spins at the three sites of a triangle. Summed over four sets of triangles and divided by 8π,

$$\rho_{sk} = \frac{1}{8\pi} \sum_{i=1}^{4} \Omega_i \tag{7}$$

is the skyrmion density at the $\mathbf{r}$ point. The skyrmion number in Fig. 1(f) is obtained by summing the lattice skyrmion density over all lattice sites in the xy plane and averaging over different xy planes. Ensemble average of the skyrmion number is performed over 300 000 MC steps.

A suitable discretization of the divergence $\partial_\alpha [\rho_{sk}^\alpha]_{3D}$ on a lattice is necessary to read off the monopole locations from a given magnetization structure. In the cubic lattice, each elementary cube consists of eight spins. Each face of the cube is divided into two triangles with three spins for each triangle. Solid angles subtended by each set of three spins were calculated using Eq. (6). Finally, all solid angles from the six faces of the cube, 12 triangles in total, were summed and divided by 4π to give the monopole number contained in this cube. The resulting monopole number is either 0, $+1$ (monopole), or -1 (antimonopole). No other number was ever found from the spin structure. Monopole locations are easily identified as the cubes with nonzero integers. We have established that both the skyrmion number and the monopole number rise and disappear at the same critical fields, i.e., they exist over the same field ranges $B_{c_1} \leqslant B \leqslant B_{c_2}$ as shown in Fig. 1(f). The average over all the layers in one MC step, and the ensemble average over 300 000 MC steps, are calculated to obtain monopole and antimonopole numbers.

C. GPU-based Monte Carlo simulations

We adopt the Buhrandt-Fritz model [19] including the ferromagnetic and DM interactions for nearest and

next-nearest neighbors, and the Zeeman term:

$$
\begin{aligned}
\mathcal{H} = {} & -J \sum_{\mathbf{r}} \mathbf{n_r} \cdot (\mathbf{n_{r+\hat{x}}} + \mathbf{n_{r+\hat{y}}} + \mathbf{n_{r+\hat{z}}}) \\
& + \frac{J}{16} \sum_{\mathbf{r}} \mathbf{n_r} \cdot (\mathbf{n_{r+2\hat{x}}} + \mathbf{n_{r+2\hat{y}}} + \mathbf{n_{r+2\hat{z}}}) \\
& - D \sum_{\mathbf{r}} \mathbf{n_r} \cdot (\mathbf{n_{r+\hat{x}}} \times \hat{x} + \mathbf{n_{r+\hat{y}}} \times \hat{y} + \mathbf{n_{r+\hat{z}}} \times \hat{z}) \\
& + \frac{D}{8} \sum_{\mathbf{r}} \mathbf{n_r} \cdot (\mathbf{n_{r+2\hat{x}}} \times \hat{x} + \mathbf{n_{r+2\hat{y}}} \times \hat{y} + \mathbf{n_{r+2\hat{z}}} \times \hat{z}) \\
& - \mathbf{B} \cdot \sum_{\mathbf{r}} \mathbf{n_r}.
\end{aligned}
\tag{8}
$$

Each spin $\mathbf{n_r}$ is a classical unit vector defined at the sites of the cubic lattice. The external magnetic field $\mathbf{B}$ is applied along the z direction. The ground state of this model at $\mathbf{B} = 0$ has the (111) spiral structure with the wave number $q = |\mathbf{q}|/\sqrt{3}$ for the x, y, and z directions given by the equation

$$
\frac{D}{J} = \frac{\sqrt{3} \sin q (4 - \cos q)}{4 \cos q - \cos 2q}.
\tag{9}
$$

We use this equation to determine the ratio D/J for the desired spiral period $\lambda = 2\pi/q$.

All Monte Carlo calculations were performed on a cubic lattice of size L^3 with periodic boundary conditions. L was chosen to be commensurate with the expected helix period. In particular, we choose $L = 30$ for $\lambda = 6, 10$ and $L = 32$ for $\lambda = 8$. Following the previous work [19], three different kinds of MC simulations were performed in order to obtain the thermodynamically stable state. They are the fixed-field annealing, and the fixed-temperature field-decreasing and field-increasing simulations. In the fixed-field annealing simulation, the magnetic-field range was divided into 30 steps from $B = 3J$ to $B = 0$. At each field, the temperature was successively lowered over 40 annealing steps for $\lambda = 8, 10$, and 160 steps for $\lambda = 6$, ranging from $T = 4.01J$ to $T = 0.01J$. Random initial configurations were adopted at the highest temperature. For the fixed-temperature, field-decreasing (increasing) simulation, we started with spin configurations obtained from the earlier fixed-field annealing procedure at high (low) field and gradually lowered (raised) the external magnetic field over 30 steps. After all the simulations were finished, we identified the state with the lowest free energy among the three annealing processes, for every temperature and field value.

MC simulations for three-dimensional lattices are very computer intensive. Instead of running the program on individual central processing units handling less than ten threads per processor, we used the general-purpose computing on graphics processing unit method, utilizing the compute unified device architecture. Several thousands of threads could run at the same time with this method. A synchronization problem occurs during the parallelization of the MC calculation among the threads. When one thread is proposing a local MC update for a spin, other threads, running at the same time, might change the surrounding spins. The exchange energy obtained in this way is not guaranteed to be correct. This problem can be avoided using the two-color checkerboard algorithm [24],

if there were only nearest-neighbor interactions. To handle next-nearest-neighbor interactions in Eq. (8), we used a three-color algorithm wherein each lattice site with the coordinates (i_x, i_y, i_z) ($0 \leqslant i_x, i_y, i_z \leqslant L - 1$) is colored by the remainder $c = (i_x + i_y + i_z) \bmod 3$. During one MC step, we performed parallel MC simulations in the order of $c = 0$, $c = 1$, and $c = 2$. All threads were synchronized after simulations over all three colors.

III. COLLECTIVE DYNAMICS OF THE MONOPOLE LATTICE

Low-frequency collective modes of the two-dimensional skyrmion lattice are well understood theoretically [25–27] and have been demonstrated by microwave experiments [28–30]. They arise from either the internal mode (each skyrmion undergoing a periodic shape deformation or in a breathing mode) or the small cyclotronlike motion of the center of mass of the skyrmions. The latter mode is the analog of phonon excitations in a crystal. With the expected characteristic exchange energy $J \sim 1$ meV and the frequency $f = J/h \sim 240$ GHz in most chiral magnet materials [25,28], collective modes have been found at a small fraction of this frequency around a few gigahertz [29,30]. A number of internal modes corresponding to zero wave vector excitation has been predicted theoretically [25–27] and observed [28–30]. It comes as a surprise that our LLG analysis reveals *only one collective mode* at zero wave vector in low frequencies $\omega \lesssim J/\hbar$.

To study the time-dependent spin dynamics excited by a magnetic-field pulse, we numerically solve the LLG equation

$$
\dot{\mathbf{n}}_{\mathbf{r}} = \frac{1}{1 + \alpha^2} \left[\frac{\delta \mathcal{H}}{\delta \mathbf{n_r}} \times \mathbf{n_r} + \alpha \mathbf{n_r} \times \left(\mathbf{n_r} \times \frac{\delta \mathcal{H}}{\delta \mathbf{n_r}} \right) \right],
\tag{10}
$$

for the 24^3 and 30^3 cubic lattices in the M phase, using the fourth-order Runge-Kutta method. Here, $\alpha = 0.04$ is the Gilbert damping constant and we choose the time unit $t_0 = \hbar/J$ to make Eq. (10) dimensionless. First, we use the MC-generated spin configuration obtained at the white box in the phase diagram Fig. 1(c) as the initial configuration of the LLG dynamics. Running the LLG calculation for a sufficiently long time relaxes the spin configuration to the stationary state $\dot{\mathbf{n}}_{\mathbf{r}} = 0$. After the relaxation, an additional magnetic-field pulse $\mathbf{B}_0 \delta(t)$ was applied in either y or z direction to excite the MAM lattice. The subsequent time evolution is obtained by solving the LLG equation. The fast Fourier transform of the magnetization curve along the y direction is used to calculate the ac susceptibility χ_y, defined by

$$
\chi_y(\omega) = \int_0^\infty e^{i\omega t} n_y(t) dt,
\tag{11}
$$

and shown as Fig. 2(a). Both real and imaginary parts of $\chi_y(\omega)$ are displayed. Here $n_y(t)$ refers to the space-averaged y component of the magnetization vector perpendicular to the external field in the z direction. A single resonance peak at $\omega_R \sim 0.03 J/\hbar$ was found. Other peaks in $\chi_y(\omega)$ exist, but at much higher frequencies $\omega > J/\hbar$. On the other hand, we found no low-energy absorption peaks in $\chi_z(\omega)$ when the pulse is applied parallel to the Zeeman field, $\delta B_z(t) = B_0 \delta(t)$. With these observations we conclude that there exists only one low-frequency internal collective mode for the MAM crystal,
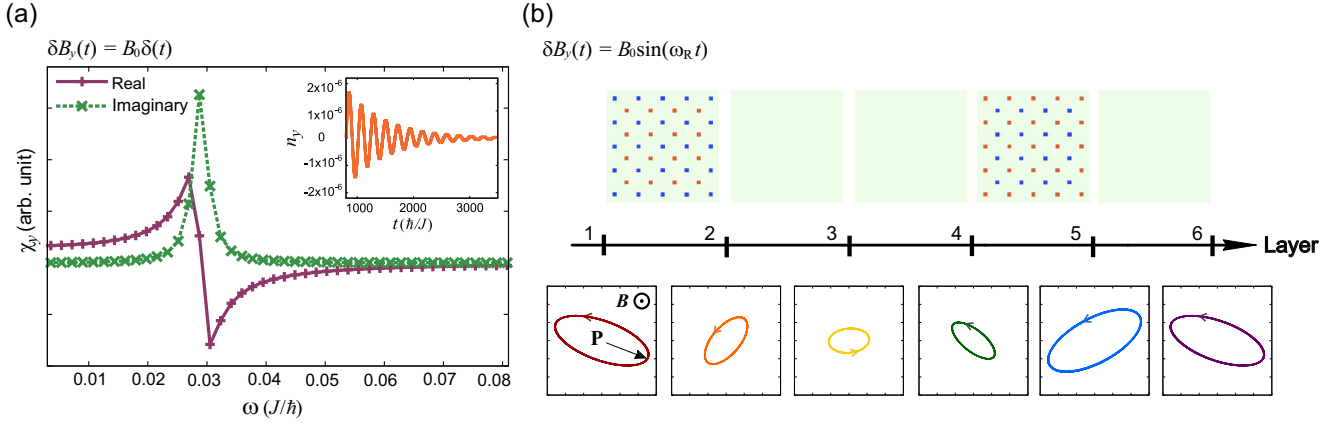
FIG. 2. Collective mode of the topological lattice. (a) Real and imaginary parts of the Fourier spectrum $\chi_y(\omega) = \int_0^\infty e^{i\omega t} n_y(t) dt$, which characterizes the response of the averaged magnetization along the y direction $n_y(t)$, to the pulsed field $B_0 \delta(t)$ applied along the y axis, $B_0/E_{DM} = 0.0023$. Resonance is observed around the frequency $\omega_R \sim 0.03 J/\hbar$. The inset shows the time-domain dynamics of $n_y(t)$. (b) Oscillation trajectories of the **P** vector (see text for definition) in several layers along the z direction, under the periodic pulse $\delta B_y(t) = B_0 \sin(\omega_R t)$, $B_0/E_{DM} = 0.023$. The sense of rotation of the **P** vector is shown with arrows. Monopoles (red squares) and antimonopoles (blue squares) are located at the dual cubic lattice positions and appear between layers 1 and 2, and also between layers 4 and 5. The whole structure, both the monopole locations and the **P**-vector trajectories, is repeated with period 5 along the z direction. In-plane monopole spacing is 6. Simulations of the Landau-Lifshitz-Gilbert equation were performed on the $L = 30$ cubic lattice.

even though earlier work on the internal excitations of the 2D skyrmions found a number of low-energy modes [25,26]. It will be nice to do an experimental check on this prediction regarding the number of collective modes.

Since the same pulse field is applied for all the sites simultaneously, the perturbation carries zero momentum and cannot couple to a phonon mode. To understand the nature of the collective excitation better we applied a sinusoidal magnetic field $B_y(t) = B_0 \sin(\omega_R t)$ at the resonant frequency and examined the time evolution of the magnetization vector $\mathbf{n_r}(t)$. From the obtained magnetization profile $\mathbf{n_r}(t)$ one can keep track of the monopole positions and the skyrmion density variations over time. First of all, the monopole and anti-monopole positions of the cube for which the monopole charge is $+1$ and -1 are strictly a constant of time either for a pulse field or a sinusoidal one, consistent with the zero-momentum nature of the perturbation. A small magnitude of the pulse field $|\mathbf{B}_0| = 0.01 J$ or the periodic field $|\mathbf{B}_0| = 0.1 J$ was used in the calculation to minimize the disturbance to the MAM crystal, while the external magnetic field was held at a much bigger value $B = 1.7 J$.

Real-time calculations for the two-dimensional skyrmion lattice in the past assumed a large skyrmion radius [25,28,29]. The slow collective motion of 2D skyrmion was easy to identify, typically by visual inspection of the real-time video generated from solving the LLG equation. Sometimes a linear interpolation scheme is used to render the information from the LLG calculation more continuous [31]. In visualizing the low-energy dynamics of the monopole crystal, however, we run into difficulties due to the small monopole size. With the typical monopole diameter of five to six lattice constants, watching the real-time spin dynamics gave very little insight into the nature of the collective mode. Further complicating the analysis is the fact that the visualization process must be done layer by layer and somehow combined into a single 3D picture mentally. After much experimentation, we arrived at

the following quantity as the best characterization tool of the collective dynamics in a layer-by-layer fashion. We call this the *skyrmion dipole vector*:

$$\mathbf{P}(z,t) = \sum_{\mathbf{r}_\perp = (x,y)} \left[\rho_{sk}^z(\mathbf{r}_\perp, z, t) - \overline{\rho_{sk}^z(\mathbf{r}_\perp, z, t)} \right] \mathbf{r}_\perp. \quad (12)$$

As one can see in this definition, the dipole vector is defined for each layer with coordinate z and, as shown in Fig. 2, does exhibit a continuous, oscillatory motion over time.

In the definition of skyrmion dipole vector (12),

$$\rho_{sk}^z(\mathbf{r}_\perp, z, t) = \frac{1}{4\pi} \mathbf{n_r}(t) \cdot [\partial_x \mathbf{n_r}(t) \times \partial_y \mathbf{n_r}(t)]$$

refers to the skyrmion density in the xy plane at a given time t. As we know from elementary physics, the definition of the dipole moment suffers from ambiguity under the arbitrary translation of the lattice vector $\mathbf{r} \rightarrow \mathbf{r} + \mathbf{r}_0$ ($\mathbf{r}_0$ = arbitrary vector), unless the total "topological charge" is zero. To remedy this problem we subtract the time-averaged skyrmion density $\overline{\rho_{sk}^z(\mathbf{r}_\perp, z, t)}$, which is the average over several time periods of $\rho_{sk}^z(\mathbf{r}_\perp, z, t)$ for each lattice site $(\mathbf{r}_\perp, z)$. Under a periodic magnetic-field perturbation $\delta B_y(t) = B_0 \sin(\omega_R t)$, each z layer develops a nonzero skyrmion dipole vector $\mathbf{P}(z,t)$, which oscillates with the resonant frequency ω_R. Figure 2(b) shows the **P**-vector trajectories for different layers forming elliptic orbits of different orientations and sizes. The elongated shape of the orbit is due to the pulse applied in the y direction that breaks the square lattice symmetry. Note the centers of monopoles are located at the dual lattice sites, or between the layers of the original cubic lattice. In Fig. 2(b) we plot the monopole and antimonopole locations found from MC calculation for the $L = 30$ cubic lattice. It is seen that monopoles and antimonopoles form between layers 1 and 2 of the original cubic lattice, and also between layers 4 and 5. The periodicity of the monopole lattice in the z direction is 5, while it is 6 in the xy plane (presumably due to the anisotropy

induced by the Zeeman field). As shown in Fig. 2(b), **P** vectors for layers immediately above and immediately below the monopole layer oscillate at roughly right angles.

IV. CONCLUSION

Both skyrmions and monopoles are physical realizations of the integer-valued homotopy group $\pi_2(S^2)$. Yet their properties differ in that the skyrmion is a smooth texture in two spatial dimensions, while the monopole is a singular object (at its center) embedded in three-dimensional space. Due to the singular nature of the monopole texture, it has been harder to find instances of its physical realization in condensed matter systems. Finally we are on the brink of claiming its realization and observation in a specific material MnGe [12,13,18], and an understanding of their physical properties becomes of prominent importance. Existing theories are of Ginzburg-Landau nature [15,17] and cannot address dynamic properties. We have demonstrated here that a simple lattice model for chiral magnets, already known to yield the two-dimensional skyrmion crystal phase at large helix periods, can also yield the monopole crystal phase by tuning the helix period to a smaller value. The low-energy collective behavior in the M phase was examined numerically, with the conclusion that only one collective mode is observable at frequencies well below $J/\hbar$. Due to the finite-size constraint in MC simulations we can only tune the helix period discontinuously, and conclude that the period $\lambda = 6$ definitely supports the monopole crystal phase even at low temperature. To compare with experiments,

we adopt the known lattice constant 4.79 Å for MnGe [32] to translate the period $\lambda = 6$ to 2.8 nm, which is slightly smaller than the experimentally determined spiral period of 3–6 nm for this material. A search for candidate materials with even shorter helix period will be in favor of realizing the three-dimensional topological phase in a more robust manner.

The remaining question is why in the F phase at finite temperature of Figs. 1(a)–1(c) one sees a nonzero density of skyrmions. We believe this is a signature of the skyrmion liquid phase [33] being realized in those temperature and field regimes. As our main focus of the paper is on the demonstration of the monopole crystal phase and its low-energy dynamics, we have not carried out extensive analysis of the possible skyrmion liquid behavior. An understanding of the underlying physics of the skyrmion liquid phase in three dimensions is an exciting future topic. Electronic structure coupled to the MAM crystal structure is also expected to yield enormously interesting physics. One simple implication of the monopole formation is that it tends to trap a localized state of the electron [34].

[1] W. Thomson, P. Roy. Soc. Edinburgh **6**, 94 (1869).

[2] T. Skyrme, Nucl. Phys. **31**, 556 (1962).

[3] S. Mühlbauer, B. Binz, F. Jonietz, C. Pfleiderer, A. Rosch, A. Neubauer, R. Georgii, and P. Böni, Science **323**, 915 (2009).

[4] S. D. Yi, S. Onoda, N. Nagaosa, and J. H. Han, Phys. Rev. B **80**, 054416 (2009).

[5] X. Z. Yu, Y. Onose, N. Kanazawa, J. H. Park, J. H. Han, Y. Matsui, N. Nagaosa, and Y. Tokura, Nature (London) **465**, 901 (2010).

[6] S. Heinze, K. von Bergmann, M. Menzel, J. Brede, A. Kubetzka, R. Wiesendanger, G. Bihlmayer, and S. Blugel, Nat. Phys. **7**, 713 (2011).

[7] S. Seki, X. Z. Yu, S. Ishiwata, and Y. Tokura, Science **336**, 198 (2012).

[8] Y. Nahas, S. Prokhorenko, L. Louis, Z. Gui, I. Kornev, and L. Bellaiche, Nat. Commun. **6**, 8542 (2015).

[9] J. H. Han, J. Zang, Z. Yang, J.-H. Park, and N. Nagaosa, Phys. Rev. B **82**, 094429 (2010).

[10] K. Harada, T. Matsuda, J. Bonevich, M. Igarashi, S. Kondo, G. Pozzi, U. Kawabe, and A. Tonomura, Nature (London) **360**, 51 (1992).

[11] C. Castelnovo, R. Moessner, and S. L. Sondhi, Nature (London) **451**, 42 (2008).

[12] N. Kanazawa, Y. Onose, T. Arima, D. Okuyama, K. Ohoyama, S. Wakimoto, K. Kakurai, S. Ishiwata, and Y. Tokura, Phys. Rev. Lett. **106**, 156603 (2011).

[13] Y. Shiomi, N. Kanazawa, K. Shibata, Y. Onose, and Y. Tokura, Phys. Rev. B **88**, 064409 (2013).

[14] S. Da Col, S. Jamet, N. Rougemaille, A. Locatelli, T. O. Mentes, B. S. Burgos, R. Afid, M. Darques, L. Cagnon, J. C. Toussaint *et al.*, Phys. Rev. B **89**, 180405 (2014).

[15] B. Binz, A. Vishwanath, and V. Aji, Phys. Rev. Lett. **96**, 207202 (2006).

[16] C. Pfleiderer, D. Reznik, L. Pintschovius, H. v. Lohneysen, M. Garst, and A. Rosch, Nature (London) **427**, 227 (2004).

[17] J.-H. Park and J. H. Han, Phys. Rev. B **83**, 184406 (2011).

[18] T. Tanigaki, K. Shibata, N. Kanazawa, X. Yu, Y. Onose, H. S. Park, D. Shindo, and Y. Tokura, Nano Lett. **15**, 5438 (2015).

[19] S. Buhrandt and L. Fritz, Phys. Rev. B **88**, 195137 (2013).

[20] X. Z. Yu, N. Kanazawa, Y. Onose, K. Kimoto, W. Z. Zhang, S. Ishiwata, Y. Matsui, and Y. Tokura, Nat. Mater. **10**, 106 (2011).

[21] P. Milde, D. Köhler, J. Seidel, L. M. Eng, A. Bauer, A. Chacon, J. Kindervater, S. Mühlbauer, C. Pfleiderer, S. Buhrandt *et al.*, Science **340**, 1076 (2013).

[22] C. Schütte and A. Rosch, Phys. Rev. B **90**, 174432 (2014).

[23] A. van Oosterom and J. Strackee, IEEE Trans. Biomed. Eng. **BME-30**, 125 (1983).

[24] T. Preis, P. Virnau, W. Paul, and J. J. Schneider, J. Comput. Phys. **228**, 4468 (2009).

[25] M. Mochizuki, Phys. Rev. Lett. **108**, 017601 (2012).

[26] Y.-H. Liu, Y.-Q. Li, and J. H. Han, Phys. Rev. B **87**, 100402 (2013).

[27] S.-Z. Lin, C. D. Batista, and A. Saxena, Phys. Rev. B **89**, 024415 (2014).

[28] W. Wang, M. Beg, B. Zhang, W. Kuch, and H. Fangohr, Phys. Rev. B **92**, 020403 (2015).

[29] Y. Okamura, F. Kagawa, M. Mochizuki, M. Kubota, S. Seki, S. Ishiwata, M. Kawasaki, Y. Onose, and Y. Tokura, Nat. Commun. **4**, 2391 (2013).

[30] Y. Onose, Y. Okamura, S. Seki, S. Ishiwata, and Y. Tokura, Phys. Rev. Lett. **109**, 037603 (2012).

[31] I. Makhfudz, B. Krüger, and O. Tchernyshyov, Phys. Rev. Lett. **109**, 217201 (2012).

[32] O. L. Makarova, A. V. Tsvyashchenko, G. Andre, F. Porcher, L. N. Fomicheva, N. Rey, and I. Mirebeau, Phys. Rev. B **85**, 205205 (2012).

[33] C. Pappas, E. Lelièvre-Berna, P. Bentley, P. Falus, P. Fouquet, and B. Farago, Phys. Rev. B **83**, 224405 (2011).

[34] S.-Y. Lee and J. H. Han, Phys. Rev. B **91**, 245121 (2015).